

Reversible gels of patchy particles: Role of the valence

John Russo,^{1,a)} Piero Tartaglia,² and Francesco Sciortino¹¹*Dipartimento di Fisica and INFM-CNR-SOFT, Università di Roma La Sapienza, Piazzale A. Moro 2, 00185 Roma, Italy*²*Dipartimento di Fisica and INFM-CNR-SMC, Università di Roma La Sapienza, Piazzale A. Moro 2, 00185 Roma, Italy*

(Received 12 January 2009; accepted 20 May 2009; published online 2 July 2009)

We simulate a binary mixture of colloidal patchy particles with two and three patches, respectively, for several relative concentrations and hence relative average valences. For these limited-valence systems, it is possible to reach low temperatures, where the lifetime of the patch-patch interactions becomes longer than the observation time without encountering phase separation in a colloid-poor (gas) and a colloid rich (liquid) phase. The resulting arrested state is a fully connected long-lived network where particles with three patches provide the branching points connecting chains of two-patch particles. We investigate the effect of the valence on the structural and dynamic properties of the resulting gel and attempt to provide a theoretical description of the formation and of the resulting gel structure based on a combination of the Wertheim theory for associated liquids and the Flory–Stockmayer approach for modeling chemical gelation. © 2009 American Institute of Physics. [DOI: 10.1063/1.3153843]

I. INTRODUCTION

In the last years, we have witnessed the development of several models for describing the process of colloidal (reversible) gel formation and the resulting gel structure and dynamics.^{1–5} It has clearly emerged that colloidal gels can result from several distinct preparation routes⁵ and an effort has been performed to identify the connections between the particle-particle interaction potential and the resulting properties of the low-density arrested state.⁶ In the case of colloidal solutions in which particle attraction is driven by depletion, gels result from an arrested phase separation and the final structure of the gel is characterized by density fluctuations with a specific wavelength, determined by the depth of the quench in the unstable region.^{7,8} In the case of particles interacting via a competing short-range attraction and a screened longer range repulsion (often of electrostatic origin), one observes one dimensional growth of the aggregates with occasional thermally driven branching which favors the formation of a spanning three-dimensional network.^{9–15} In other colloidal systems, the possibility of independently tuning number and lifetime of the bonds provides a case where gelation may even coincide with geometrical percolation.^{4,16–18}

An additional important mechanism of gel formation is offered by the so-called reduced (or limited) valence, i.e., by the collective behavior of particles interacting with dominant directional interactions, limiting the possibility of forming bonds with neighboring particles.¹ The study of the phase diagram of these particles as a function of the valence has shown that the region in which phase separation in a colloid-poor (gas) and a colloid rich (liquid) phase is observed progressively shrinks on decreasing the valence, vanishing for

valence approaching two.^{19–21} Hence, for small valences, it is possible to explore low-density states at low temperatures (where the bond lifetime is significantly large) without encountering phase separation. These low temperature T -low packing fraction ϕ states have been named equilibrium gels, since the gel state can be approached continuously from high temperatures without encountering any phase transition.²² Studies of models with limited valence^{23,24} are also relevant in the promising field of patchy and functionalized particles²⁵ as well as in modeling irreversible aggregation in colloidal particles with limited valence^{26–30} or in developing connections between reversible and irreversible gelations.³¹

Systems with small limited valence are particularly interesting since they are amenable to analytic modeling.^{19–21,32} Indeed, for a binary mixture of particles with valence two and three, when the average valence per particle is close to two, the static equilibrium properties of limited-valence colloids have been successfully described by a combination of the Wertheim (W) theory for associating liquids^{33,34} and the Flory–Stockmayer (FS) approach for chemical gelation.³⁵ Here we extend such analysis to examine the effect of the valence on the structure of the equilibrium gels by investigating at a specific value of packing fraction of $\phi=0.1$ a two-component system made of bifunctional and three-functional particles for several relative concentrations, corresponding to average valence ranging from 2.1 to the largest possible value for which phase separation is not encountered on cooling, i.e., ≈ 2.8 . This study offers us the possibility to examine the effect of the valence on the static and dynamic properties of the resulting gel and to investigate the range of validity of the W and FS theories in modeling gel formation in this class of colloids. We focus our attention on how the dynamics of the fully connected low T gel is affected by the average valence.

The paper is organized as follows. Section II introduces

^{a)}Electronic mail: john.russo@roma1.infn.it.

the model and gives a brief account on the relevant aspects of W and FS theories. Section III compares the W-FS predictions with the results from simulations, showing also the limits of its applicability. Section IV concentrates on the static and dynamic properties of the low temperature systems in the absence of bond breaking processes. We conclude our work in Sec. V, where possible directions for future studies are presented.

II. MODEL AND COMPUTATIONAL DETAILS

A. The interaction potential

We aim at modeling particles where the dominant attractive interaction is highly directional or patchy. We limit ourselves to cases where each patch can be engaged in only one bond, the so-called single bond per patch condition, in such a way that the maximum number of possible bonds which can be formed is encoded in the choice of the particles and it can be tuned by changing the relative concentrations of particles with different number of patches. A particle i is modeled as a rigid body defined by the position of its center of mass and by a number M_i of vectors indicating the locations of the M_i patches. Patches are located at distance 0.5 from the particle's center of mass. The interaction potential between particles 1 and 2 is

$$V(1,2) = V_{\text{CM}} + V_P, \quad (1)$$

where V_{CM} is the potential acting between the centers of mass of the two particles and V_P is the interaction between patches. Different from previous studies based on stepwise potentials, we study here the case of a continuous potential by choosing

$$V_{\text{CM}}(12) = \left(\frac{1}{r_{12}} \right)^m, \quad (2)$$

$$V_P(12) = - \sum_{i=1}^{M_1} \sum_{j=1}^{M_2} \epsilon \exp \left[- \frac{1}{2} \left(\frac{r_{12}^{ij}}{\alpha} \right)^n \right], \quad (3)$$

where $m=200$ is chosen to approximate the hard-sphere behavior; $n=10$, so that the exponential function resembles a square well; $\alpha=0.12$ to fulfill the single bond per patch condition and $\epsilon=1.001$ to impose that the absolute minimum is at unitary depth. Moreover, r_{12} is the distance between particles 1 and 2 center of mass, r_{12}^{ij} is the distance between patches i and j on different particles, and M_1 and M_2 are the number of patches of particles 1 and 2, respectively. Bond forces thus act on patches allowing momenta which can induce rotations of the monomers.

The parameters entering in the functional form [Eqs. (2) and (3)] have been chosen in such a way that the resulting potential has a depth of $u_0=-1$ and it resembles the hard sphere plus square well potential, allowing greater flexibility in the study of the dynamics of these systems compared to stepwise potentials. Figure 1 shows the specific shape of the interaction potential for two particles approaching each other in the best bonding geometry, i.e., when the two patch sites face each other. The short range attractive potential, Eq. (3), guarantees that each patch is engaged at most in one bond.

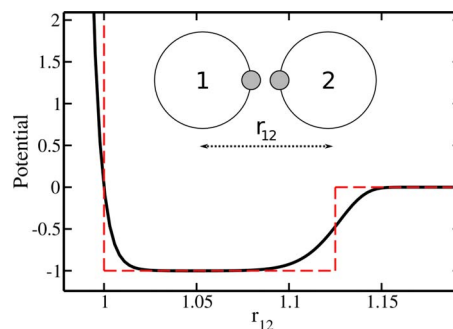


FIG. 1. Graphic representation of the potential. Solid (black) line represents the potential of Eq. (1) when colloids 1 and 2 approach, as shown in the inset. The chosen potential is the continuous version of the hard sphere + square well potential depicted with a dotted (red) line.

B. Numerical details

We study a binary mixture composed of N_2 particles with two patches (bifunctional) and N_3 particles with three (three functional) with $N=N_2+N_3=1000$ for several values of $x_2 \equiv N_2/N$. For bifunctional particles, the two sites (patches) have been located on the poles, while for the three-functional particles, the three sites have been equally spaced on the equator. In some cases, simulations have been performed for $N=8000$ to estimate size effects. Five different values of the average valence $\langle M \rangle \equiv (2N_2 + 3N_3)/N = 3 - x_2$ have been studied, varying in the range of 2.1–2.8, where the upper limit is fixed by the constraint of avoiding phase separation at low temperature at the chosen ϕ . We have performed Brownian dynamics simulations with the algorithm described in the Appendix. In the following, the energy unit is chosen to be the depth ϵ of the potential, distances are in units of the colloids diameter (σ), time is in units of $\sigma \sqrt{m/\epsilon}$, where m is the mass of the colloid. Temperature is also measured in unit of energy (Boltzmann constant $k_B=1$). The integration time step used is 10^{-3} units of time. In these units, the chosen translational diffusion coefficient is $D_T=0.01$ and the corresponding rotational diffusion coefficient is $D_R=0.03$ (so that $D_R/D_T=3$, as expected for nonslip particles). For a colloidal particle with diameter of $1 \mu\text{m}$ in water at ambient T (kinematic viscosity $\nu=1 \text{ mm}^2/\text{s}$), the unit of time would correspond to 22.8 ms and the particle would thus diffuse a distance equal to its diameter in a time of 16.6 , corresponding to a physical time of 0.38 s. We thus define the time scale as $\tilde{t}=t/16.6$, with $\tilde{t}=1$ being the time a free particle needs to diffuse a distance equals to its diameter.

We have equilibrated configurations at four different temperatures ($T=0.09, 0.07, 0.06, 0.055$), monitoring the approach of the potential energy to its long time value. Equilibrium runs have been performed for more than $5 \cdot 10^8$ integration time steps (corresponding to several months of computer time) to produce the necessary trajectories. Note that the probability of breaking a bond is $\sim e^{1/k_B T}$. At $T=0.055$ this term is already of the order of 10^8 , explaining the need for very long simulations to be able to explore several breaking and reforming events. The equilibrium configurations at $T=0.055$ have been cooled down to $T=0.04$ and we have waited until all small isolated clusters have attached to the spanning one. This is equivalent to perform-

ing a quench from randomly distributed monomers since it has been recently shown that for low-valence patchy systems the aging process proceeds through equilibrium states.³⁶ Hence, at this low T all particles belong to the same cluster and never detach from it. The only possible dynamics concern modes which do not alter the system connectivity.

C. Wertheim theory

The W theory^{33,37,38} provides a route to evaluate the probability p_b that a patch is engaged in a bond. It requires only information on the interaction bonding potential and the reference isotropic interaction. More specifically,

$$\frac{p_b}{(1-p_b)^2} = \langle M \rangle \rho \Delta, \quad (4)$$

where $\langle M \rangle$ is the average number of patches per colloid, ρ is the system number density, and Δ is defined by

$$\Delta = 4\pi \int g_{CM}(r_{12}) \langle f(12) \rangle_{\omega_1 \omega_2} r_{12}^2 dr_{12}. \quad (5)$$

Here, $g_{CM}(r_{12})$ is the pair correlation function of a reference fluid whose potential is V_{CM} , Eq. (2), and $\langle f(12) \rangle_{\omega_1 \omega_2}$ represents an angle average over all orientation of particles 1 and 2 at a fixed relative distance r_{12} of the Mayer function, $f(12) = \exp(-V_P(r_{12}^i)/k_B T) - 1$. Equation (4) is equivalent to the mass-action law formulation of the chemical equilibrium between bonded and not-bonded independent sites.³⁹ The calculation of the averaged Mayer function is performed numerically via a Monte Carlo integration algorithm. An expression of the pair correlation function $g_{CM}(r_{12})$ is then needed in the range where bonding occurs. This function is obtained by numerical simulation of the V_{CM} model. Before integration, the numerical $g_{CM}(r_{12})$ is smoothed with a spline under tension interpolation.⁴⁰

D. Connectivity properties—Flory–Stockmayer

Reference 20 called attention on the fact that the W and the FS theories are based on the same set of approximations and hence the thermodynamic approach of W theory could be used to provide a parameter-free evaluation of the bond probability to be used in the evaluation of the T and ϕ dependence of the cluster size distributions. Within the FS approach, the percolation transition is reached when $p_b^c = 1/(1+p_3)$, where $p_3 \equiv 3N_3/(2N_2+3N_3) = 3x_3/(2+x_3)$ and $p_2 = 1-p_3$ are the probabilities that a randomly chosen site belongs to a three-functional or to a bifunctional particle. p_b can also be written as a function of the average valence as $p_b^c = \langle M \rangle / 4\langle M \rangle - 6$. Hence, the T at which the system percolates depends on $\langle M \rangle$ or equivalently on the fraction of bifunctional particles. For the chosen value of ϕ , the predicted percolation transition temperature as a function of x_2 is reported in the inset of Fig. 2. It is interesting to observe that by tuning the average valence, the percolation transition can be moved to arbitrarily small temperatures, i.e., to temperatures where the bond lifetime is significantly longer than the experimental time. Under these conditions, the system will behave as a chemical gel, where percolation coincides with

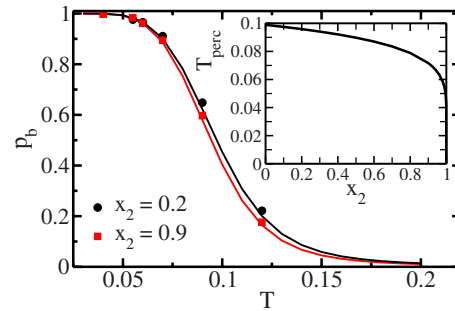


FIG. 2. Temperature dependence of the bond probability for two different average valences at $\phi=0.1$. Lines are fitting-free theoretical predictions while symbols are results of numerical simulations. The inset shows the percolation temperature T_{perc} as a function of the fraction of bifunctional monomers x_2 predicted by the FS theory.

the onset of nonergodic collective behavior. For all models with finite range of interactions,^{41,42} at the critical density, percolation via bonds always takes place at a temperature higher than the critical point temperature. Hence, in equilibrium, the percolation line is always located in the fluid region and crosses the binodal on the left side of the coexistence curve.

The FS theory also provides expressions for the cluster size distributions.³⁵ The number of clusters containing l bifunctional particles and n three-functional ones is³⁵

$$N_{nl} = N_3 \frac{(1-p_b)^2}{p_3 p_b} [p_3 p_b (1-p_b)]^n [p_2 p_b]^l w_{nl}, \quad (6)$$

$$w_{nl} = 3 \frac{(l+3n-n)!}{l! n! (n+2)!},$$

where w_{nl} is a combinatorial contribution.³⁵ Distributions are normalized in such a way that $\sum_{ln, l+n>0} (l+n) N_{nl} = N_2 + N_3$ for $p_b < p_b^c$. FS also provides expressions for the total number of finite size clusters $\#_c = \sum_{ln, l+n>0} N_{nl}$ and for the total number of bonds in finite size clusters

$$\#_{\text{bond}}^{\text{finite}} = \sum_{ln, l+n>0} (l+n-1) N_{nl}. \quad (7)$$

These expressions can be extended to $p_b > p_b^c$ in the Flory postgel assumption. This assumption, which indicates the possibility of reactions inside the infinite clusters, i.e., the formation of loops of bonds in the infinite cluster (but only there), has been shown to properly describe the case of thermoreversible gelation when $\langle M \rangle = 2.05$,²⁰ and it is worth to explore the range of its validity as a function of the average valence. Note that for $p_b > p_b^c$, $\sum_{ln, l+n>0} (l+n) N_{nl} / N = 1 - P_\infty$, where P_∞ is the fraction of particles in the infinite spanning cluster.

Before concluding this section, we recall that both W and FS theories are based on the assumption of independent bonds and on the assumption of absence of closed bond loops in finite size clusters. Under these conditions, the number of clusters $\#_c$ is given by $\#_c = N - \#_b$, since the formation of a bond links together two distinct clusters. Bond loops are found only in the infinite cluster. We also note that the num-

ber of loops in a cluster can be calculated as the difference between the number of bonds and the number of particles in the cluster (minus one).

III. NUMERICAL RESULTS FOR THE BOND PROBABILITY AND FOR THE CONNECTIVITY

The very sharp shape of the bonding potential makes it possible to unambiguously define the bond between two particles introducing a site-site distance criterion. We define as bonded any pair of particles whose site-site distance is less than 0.15σ . The bond probability is then calculated as the average number of bonds $\#_b$ found in the system divided by the maximum number of bonds possible in the system $\#_b^{\max}$, i.e.,

$$p_b = \frac{\#_{\text{bond}}}{\#_{\text{bond}}^{\max}}. \quad (8)$$

The single-bond per site condition allows us to write $\#_b^{\max} = 2N_2 + 3N_3/2$. Figure 2 shows the T dependence of p_b for two systems with different values of the average valence at $\phi=0.1$. It also shows the corresponding parameter-free predictions for p_b based on the W theory, as discussed in Sec. II C. The comparison between theory and simulation confirms^{20,43} that the W theory provides a rather accurate modeling of the thermodynamic of the system in the explored range of average valences.

The analysis of the configurations allows us to evaluate the presence of loops of bonds and to test the main assumptions of W and FS theories. Figure 3 shows in (a) the fraction of clusters with at least one bond loop inside the cluster and in (b) the average number of loops in loop-containing clusters. A clear trend toward increasing the loops with increasing the average valence is detected. For $x_2=0.9$, clusters smaller than 50 particles are not involved in loops. Even more, the number of loops is always negligible. Even very large clusters do not incorporate more than two or three bond loops. The situation is different for the case $x_2=0.2$, for which clusters of size 10 already show bond loops.

According to the FS theory bond loops are only contained in the infinite spanning cluster and it is possible to calculate the predicted average number of loops $\#_{\text{loop}}$ per particle in the spanning cluster as a function of p_b . Indicating with $\#_{\text{bond}}^{\infty}$ ($\#_{\text{bond}}^{\text{finite}}$) the number of bonds in the infinite (finite) clusters and with NP_{∞} the number of particles in the infinite cluster, then

$$\frac{\#_{\text{loop}}}{NP_{\infty}} \equiv \frac{\#_{\text{bond}}^{\infty} - (NP_{\infty} - 1)}{NP_{\infty}}, \quad (9)$$

where $\#_{\text{bond}}^{\infty} \equiv \#_{\text{bond}} - \#_{\text{bond}}^{\text{finite}}$. Both contributions can be calculated as discussed previously [Eqs. (7) and (8)], according to the FS theory. The $\#_{\text{loop}}$ per particle in the infinite cluster is a function of p_b , approaching the asymptotic limit $\#_{\text{loop}}/NP_{\infty} = x_3/2$ when $p_b \rightarrow 1$ and $P_{\infty} \rightarrow 1$, i.e., when all particles belong to the infinite cluster. Figure 3(c) compares the FS predictions with the numerical results. Deviations in this average value are only seen for the case of $x_2=0.2$ and close to percolation. For $p \gg p_b^c$ the mean field FS predictions are quite accurate for all average valences.

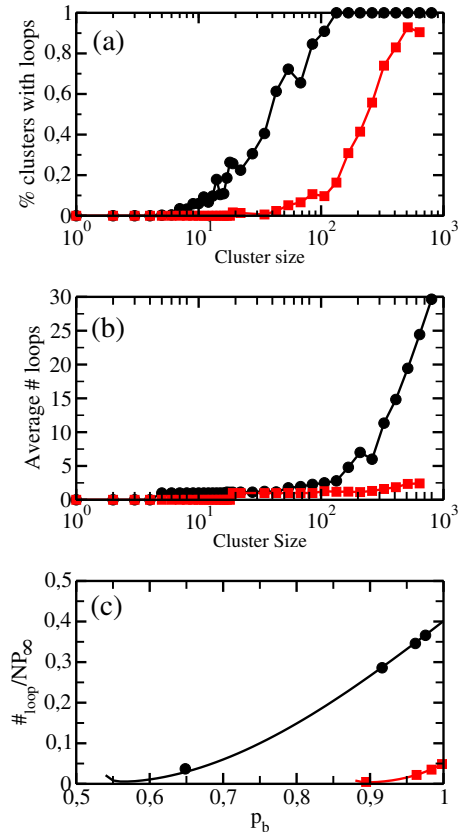


FIG. 3. Study of the presence of loops in clusters for $x_2=0.2$ (circles) and $x_2=0.9$ (squares) for, respectively, $T=0.09$ and $T=0.07$. These state points are close to the percolation transition to be able to sample a large variety of cluster sizes. (a) Fraction of clusters with at least one bond loop inside the cluster and in (b) the average number of loops in loop-containing clusters. (c) Average number of loops per particles in spanning cluster. Solid lines are the FS theory predictions (for $p_b > p_c$). For $x_2=0.2$ the theoretical predictions agree very well with the data except for the lowest p_b where the FS prediction is not as accurate.

Figure 4 shows a comparison between the cluster-size distribution $N(s)$, summing over all realization of N_{lm} [Eq. (6)] for which $l+m=s$, calculated in the theory and in simulation for two different average valence values and for state points close to percolation. The parameter-free theoretical predictions agree rather well with the numerical results for the case of $x_2=0.9$ but show detectable deviations for the case of $x_2=0.2$ in the same range of values of cluster sizes

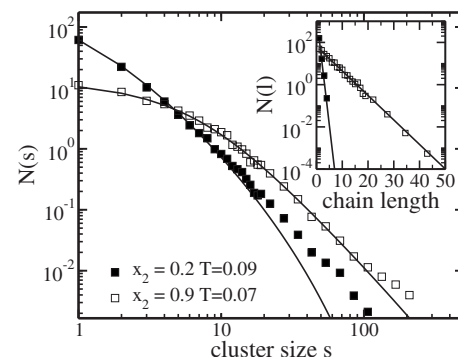


FIG. 4. Cluster size distribution close to percolation for $x_2=0.2$ ($T=0.09$) and $x_2=0.9$ ($T=0.07$). The inset shows the distribution of chain lengths in the same systems. All lines are parameter-free predictions based on the combined use of the FS-W theories.

for which intracluster bonds are present. In the percolation universality class,⁴⁴ the cluster size distribution must decay with the law $N(s) \sim s^{-\tau}$, where the critical exponent $\tau \approx 2.2$, different from the value of $\tau=2.5$ which results from the FS mean field predictions. The absence of significant amounts of bond loops and the substantial agreement of the cluster size distribution in the $x=0.9$ case confirms that the small valence plays a significant role in the stabilization of the mean-field universality class with respect to the percolation universality class,⁴⁵ locating the crossover between the two classes⁴⁶ very close to the percolation point. Hence in a very large range of p_b values, the FS predictions provide an accurate description of the connectivity properties of the system.

Particles with valence three act as junction points of chains of bifunctional particles. Within the FS theory it is possible to derive an expression for the distribution of the length of chains formed by only bifunctional particles. This is equivalent to exclude all bonds between particles with functionality three in the analysis of the connectivity or equivalently to remove all three-functional particles and analyze the resulting distributions of chains. The number of chains of length l , normalized in such a way that $\sum_{l=1}^{\infty} lN_l = N_2$, is

$$N_l = N_2(1 - p_2 p_b)^2 (p_2 p_b)^{l-1}. \quad (10)$$

The N_l distribution is thus always exponential. Again, a combined use of W and FS theories provides a very accurate description of N_l , as shown in the inset of Fig. 4.

When clusters percolate, the three-functional particles provide the branching point of the network. At small T , $p_b \rightarrow 1$ and all possible bonds are formed. The chain length distribution provides the information on the distribution of distances between the branching points, i.e., a precise characterization of the structure of the resulting fully connected network. The distribution N_l becomes controlled only by the relative fraction of two-functional particles. Indeed, in the low T limit, Eq. (10) becomes

$$N_l(T \rightarrow 0) = N_2(1 - p_2)^2 p_2^{l-1}. \quad (11)$$

Such expression can be interpreted as a growth process where, starting from a bifunctional particle connected to a three function particle (probability of $1-p_2$), a chain of $l-1$ two-functional particles is added. This is possible selecting randomly sites of type 2 for each addition in the chain. The last particles are again connected to a type 3 particle (probability of $1-p_2$). The average distance \bar{l} between branching points in the network—an indication of the mesh of the network—is $\bar{l} = \sum_l l N_l / \sum_l N_l = 1/(1-p_2)$.

Figure 5 compares the theoretical predictions for \bar{l} with the numerical results at the lowest studied T , i.e., $T=0.04$, for which essentially all bonds are indeed formed, confirming that in the explored region of valences, the structure of the resulting low T networks results from a random mixing of the particle types in agreement with the FS assumptions.

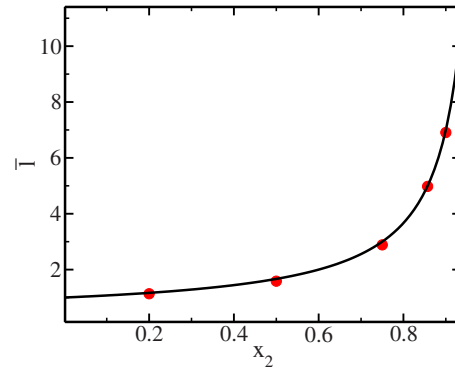


FIG. 5. Average length of the chains of bifunctional particles \bar{l} connecting the three functional branching particles in the low T fully bonded network as a function of the fraction of bifunctional one x_2 . Lines are fitting-free theoretical predictions while symbols are results of numerical simulations at $T=0.04$.

IV. THE LOW T NETWORK: PERMANENT BONDS

At $T=0.04$ the bond lifetime is much longer than the accessible observation time and p_b is very close to one ($p_b = 0.997$) so that the network is almost fully connected with particles never detaching from it. These conditions are the same as ideal chemical gels characterized by irreversible bond formation. Here we discuss both structural and dynamical properties of the low T network, emphasizing the role of the average valence.

A. Structural properties

To quantify the differences in the structure between networks with different average valence, we calculate the radial distribution function $g(r)$ independently from the particle type. The function $g(r)$ provides information on the relative location of the particles in the system. Figure 6(a) shows this function for the two limiting cases, $x_2=0.2$ and $x_2=0.9$. The $g(r)$ is significantly peaked around $r=\sigma$, an evidence of the preferential bonding distance. The peak value is significantly larger than the one observed in simple liquids, an effect due to the short range of the attractive potential, which produces a significant localization at low T . In the case of abundance of two-patch particles the sequence of following peaks is centered at distances multiple of the particle size, showing that particle chaining is dominant. In the case of $x_2=0.2$, the main peak is instead located at around 1.8σ , a position dictated by the triangular structure of the majority species, which imposes a 120° angle between the connected particles.

Figure 7 shows a slab of the system in the (almost) fully connected low T state for $x_2=0.2$ and $x_2=0.9$. Despite the fact that the ϕ is the same for both cases, the two pictures appear rather different. The necessity to satisfy all possible bonds induced by the small temperature imposes in the $x_2=0.2$ case a condensation of the three-functional particles, which can only be achieved by locally increasing the density and with the concomitant appearance of empty region, the precursors of the gas-liquid transition. In the $x_2=0.9$ case, the density of bonds is lower due to the large number of bifunctional particles and the system does not encounter any difficulty in satisfying all bonds in a homogeneous configuration.

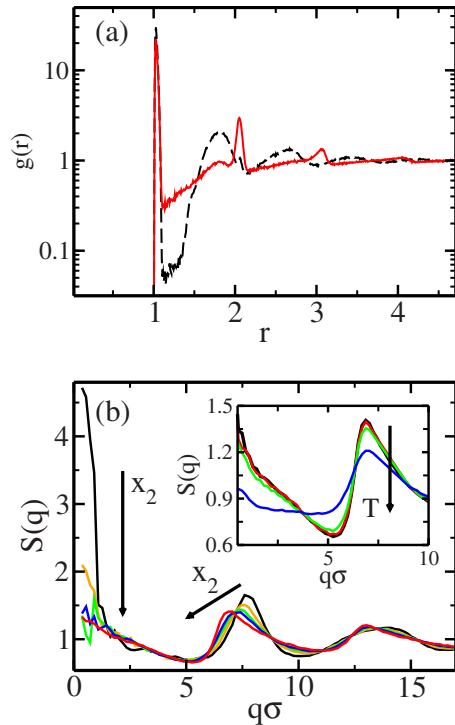


FIG. 6. (a) Radial distribution function $g(r)$ at $T=0.04$ for $x_2=0.2$ (dashed line) and for $x_2=0.9$ (solid line). The position of peaks reflects the different structure imposed by the patch geometry. (b) Particle-particle structure factor $S(q)$ for valences $x_2=0.2, 0.5, 0.66, 0.75, 0.9$. The increase at small q for large valences signals the approach to the liquid-gas instability. The inset shows the T dependence of the structure factor for the system $x_2=0.9$ for temperatures $T=0.04, 0.06, 0.070, 0.09$.

The effect of the valence on the spatial homogeneity of the sample is well captured by the behavior of the structure factor $S(q)$ [the Fourier transform of $g(r)$]. $S(q)$ can be calculated as

$$S(q) \equiv \left\langle \frac{1}{N} \sum_{i,j} e^{-i\vec{q} \cdot (\vec{r}_i - \vec{r}_j)} \right\rangle, \quad (12)$$

where \vec{q} is the exchanged wave vector, \vec{r}_i is the coordinate of particle i , the sum runs over all N particles in the system independently of their valence, and the average $\langle \dots \rangle$ is over equilibrium configurations. The structure of the low T network is shown in Fig. 6(b) for all investigated values of the average valence. The softness of the network manifests itself in the non-negligible value of $S(q)$ for small q since the $q \rightarrow 0$ limit of $S(q)$ provides a measure of the compressibility of the system. Figure 6(b) also shows that when x_2 is small, an additional increase in $S(0)$ is observed. Such large increase in $S(q)$ at small q indicates a vanishing of the compressibility and the nearby presence of a thermodynamic instability connected to the gas-liquid phase separation. Indeed, as discussed in Ref. 19, the width of the unstable region in the ϕ - T plane is controlled by the average valence, and it shrinks to zero as the average valence approaches two. Hence, at fixed ϕ , the distance from the instability increases on decreasing the valence. For each value of ϕ , there is a critical value of the valence for which phase separation is not encountered on cooling. For $\langle M \rangle$ values smaller than the

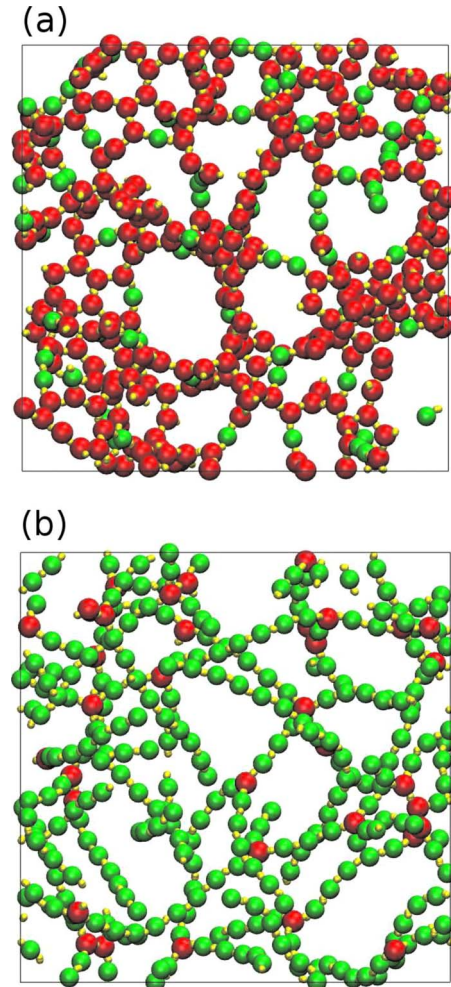


FIG. 7. Representative configurations of the gel structure at $T=0.04$ for two slabs of side 17σ and width 6σ for (a) $x_2=0.2$ and (b) $x_2=0.9$. Bifunctional particles are coded in light grey (green), three-functional particles are coded in dark grey (red), and patches are coded in light grey (yellow). Dangling ends, which can be seen, are due to the fact that just a slab of the entire system is depicted.

critical, the system always remains in homogeneous conditions on cooling. The low q behavior of $S(q)$ suggests that $x_2=0.2$ is indeed close to such critical value when $\phi=0.1$ in agreement with the direct visual inspection of the configurations previously discussed. Stable equilibrium networks can only be realized with smaller values of the average valence.

The shape of $S(q)$ close to $q\sigma \approx 2\pi$ also shows a significant dependence on the average valence. The peak becomes more and more asymmetric on increasing x_2 , an effect of the progressive chaining in the system.

The inset of Fig. 6(b) shows the temperature dependence of the structure factor for the system $x_2=0.9$. As the temperature is lowered the structure factor approaches an asymptotic low T value. This asymptotic value is reached well within the temperature region where equilibrium simulations can be performed (consistently with what has been previously observed in other models for reversible gels²). In this way, cooling one of these equilibrium low T configurations into a nonergodic system has the only effect of increasing (exponentially in $1/T$) the lifetime of bonds.

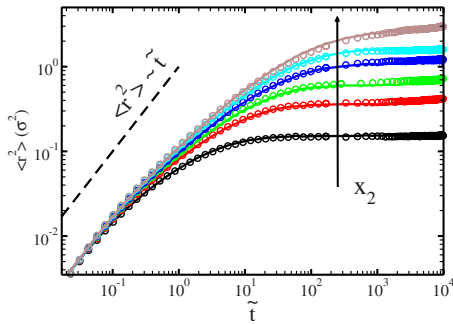


FIG. 8. Particle mean square displacement $\langle r^2 \rangle$ in the fully connected network state ($T=0.04$) for all studied x_2 values. Continuous lines are the mean square displacements of the three-functional particles. Symbols are the mean square displacement for bifunctional particles multiplied by 2/3. The dashed line shows the expected time dependence for the diffusive behavior at short times.

B. Dynamic properties

In this section we investigate the dynamics at the lowest studied $T=0.04$. In this set of simulations, bonds never break or form during the investigated time window. Moreover, all particles are connected in the same unique cluster. In this way, the observed dynamics can be attributed to the intrinsic breathing modes of the network without any masking effect due to the dynamics of small isolated clusters (or monomers) diffusing in the system (as it would be the case at slightly higher T).

1. Mean square displacement

The continuous line in Fig. 8 shows the mean square displacement of the three-functional particles as a function of the average valence. At large times, the mean square displacement shows a crossover toward a plateau value, which indicates the (squared) localization length l_o^2 of the particles in the arrested structure. l_o^2 depends sensibly from x_2 , varying more than a factor of 20 in the explored range. While in the case of a majority of three-coordinate particles the distance over which a particle can delocalize is of the order of $\approx 0.5\sigma$, it becomes $\approx 2\sigma$ in the case of $x_2=0.9$. These figures are significantly larger than the localization length observed in glasses, where a value of the order of 0.1σ is typical. The reason for such large values is due to the fact that particles are indeed confined by bonds, and hence with relative positions fixed by the connectivity of the network, still particles participate in large-amplitude breathing floppy modes involving large section of the network.^{1,2} Since the energy cost of these modes is rather small, the amplitude of the modes is rather large, determining a localization length significantly larger than the typical size of the bond. Using a terminology borrowed by the glass, the cage confining the particles is not generated by the nearest neighbors but by the connectivity of the system. The important part of the dynamics of the network is thus encoded in the crossover region, i.e., in the way particles explore the amount of space accessible in the bonded configuration. Signatures of localization and nonergodicity are thus expected only for wave vectors smaller than $2\pi/l_o$, i.e., in a region of wave vectors significantly smaller than one where nonergodicity is observed in glasses.

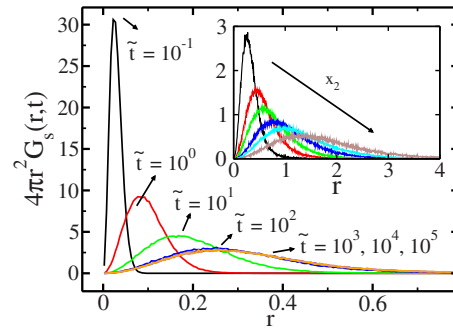


FIG. 9. Van Hove self-correlation function for the $x_2=0.2$ systems at different times. For $\tilde{t} > 10^2$, $G_s(r,t)$ remains almost time invariant since particles are caged by neighboring particles of the network gel. The inset shows the Van Hove function at $\tilde{t}=10^5$ for systems with different compositions.

An important characteristic of the low- T network is the relation between the motion of three-functional particles and bifunctional ones. Bifunctional particles compose the chains in the fully connected network while three-functional particles act as branching points or, borrowing terminology from polymer gels, as crosslinks between the chains. Surprisingly, as shown in Fig. 8, for all investigated average valences, the mean square displacement of branching points is 2/3 times the one for bifunctional particles, suggesting that the fluctuations of bi- and three-functional particles are strongly correlated and hence related to the fluctuations of the network as a whole. It is interesting to observe that the 2/3 factor is predicted by the phantom model of polymer gels.^{47,48} Such model, applied to a network composed of chains with N monomers and crosslink points of valence f , predicts that crosslinks will have Gaussian fluctuations of variance $N/f(f-2)$ while chain segments will fluctuate on average with variance $fN/6(f-2)$. The ratio between spatial fluctuations of f -functional units and bifunctional ones is then $6/f^2$, which provides the factor 2/3 for the case of $f=3$. It thus appears that despite the phantom model is valid for ideal nonoverlapping Gaussian chains, it provides a fair understanding of the relation between the fluctuations of crosslinks and chains which compose the network in the presently investigated patchy model.

C. Van Hove self-correlation function

The Van Hove self-correlation function is defined as

$$G_s(\mathbf{r}, t) = \frac{1}{N} \left\langle \sum_{i=1}^N \delta(\mathbf{r} + \mathbf{r}_i(0) - \mathbf{r}_i(t)) \right\rangle \quad (13)$$

and represents the probability distribution of finding a test particle at distance r from the origin at time t , given that the same particle was at the origin at time $t=0$. Figure 9 shows the probability $4\pi r^2 G_s(r,t)$ at various times for the system $x_2=0.2$. For $\tilde{t} < 10^2$ we observe a progressive extension of the tails of $G_s(r,t)$ as particles explore more and more space as time increases. For $\tilde{t} > 10^2$ the Van Hove function remains almost time invariant since particles are trapped in the gel network and are not allowed to diffuse. This is in fact the same time when the mean square displacement reaches its constant value (Fig. 8). The inset of Fig. 9 shows the long

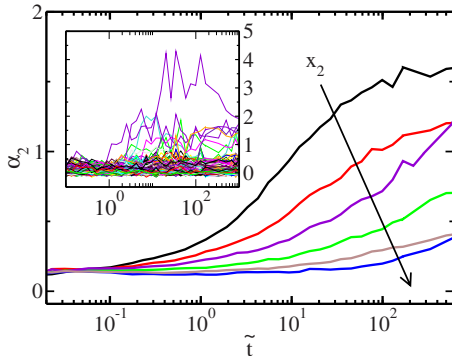


FIG. 10. Non-Gaussianity parameter α_2 as a function of time for different composition (x_2). The non-Gaussianity of the confining effective potential becomes more and more pronounced as more N_3 particles are added to the system. In this figure, α_2 has been calculated for times up to 10^3 since statistical noise in the last decade (up to 10^4) overwhelms the signal. The inset shows α_2^i , the non-Gaussianity parameter for each particle i of N_3 type for the system $x_2=0.2$.

time (and time invariant) Van Hove function for systems with different compositions. Lowering the N_3 concentration results in a broader distribution shifted at higher r . This provides the same information as the plateau height in Fig. 8 since the localization length is just the variance of the Van Hove function: $I_0^2 = \lim_{t \rightarrow \infty} \langle r^2 \rangle = \int G_s(r, t = \infty) r^2 dr$.

The shape of $G_s(r, t)$ in its time-invariant state gives useful information about the confining potential that particles feel in the network. If particles were constrained to move in a three-dimensional harmonic potential then the $G_s(r, t)$ would be a Gaussian distribution. In fact one would expect that at low T the motion of particles in the cage has a significant harmonic character. To quantify the degree of Gaussianity of the Van Hove function it is possible to study the following parameters:⁴⁹

$$\alpha_n(t) = \frac{3^n}{(2n+1)!!} \frac{\langle r^{2n}(t) \rangle}{\langle r^2(t) \rangle^n} - 1. \quad (14)$$

In particular $\alpha_2(t)$ is called the non-Gaussianity parameter since values different from zero signal a non-Gaussian shape of $G_s(r, t)$. A plot of $\alpha_2(t)$ for systems with different composition is shown in Fig. 10. It shows that after the short-time region, where $\alpha_2=0$, the non-Gaussianity of the van Hove function builds up in the “cage” regime and is more pronounced for systems with higher N_3 . Three-functional particles are thus responsible for enhancing the non-Gaussian behavior of the network oscillations.

To investigate the origin of the non-Gaussianity, in the fully connected gel, we study the non-Gaussian behavior of each single particle. Indeed the strong structural inhomogeneity which characterizes the network may well give rise to a significant value of α_2 despite the Gaussian behavior of each individual particle. To see this we write the expression of α_2 by explicitly indicating the contribution of individual particle i ,

$$\alpha_2 = \frac{3}{5} N \frac{\sum_i \langle r_i^4 \rangle}{(\sum_i \langle r_i^2 \rangle)^2} - 1. \quad (15)$$

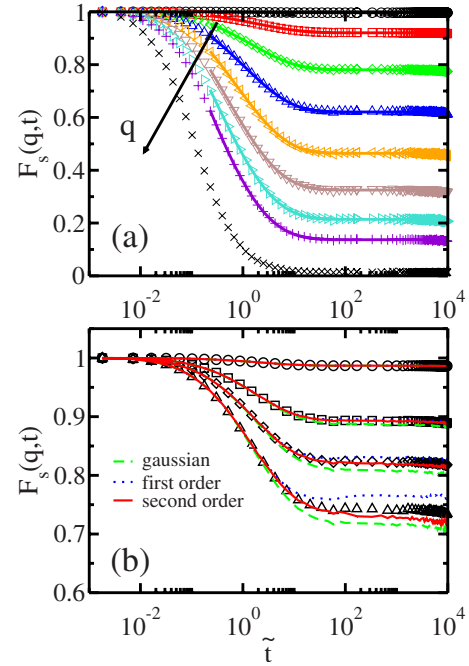


FIG. 11. (a) Tagged particle autocorrelation function in the network state ($T=0.04$) at $x_2=0.2$ for several wave vectors [$q\sigma = 0.36, 1.81, 3.26, 4.70, 6.15, 7.60, 9.04, 10.49, 16.28$]. Solid lines represent the stretched exponential fit in the region $0.2 < \tilde{t} < 10^4$. (b) Tagged particle autocorrelation function for $q\sigma=0.72$ (circles), $q\sigma=2.17$ (squares), $q\sigma=2.89$ (diamonds), and $q\sigma=3.62$ (triangles). For each data set the corresponding Gaussian approximation [dashed (green) line], first order [dotted (blue) line], and second order [solid (red) line] of Eq. (19) are represented.

The inset of Fig. 10 shows that the motion of the individual particles is rather well approximated by a diffusional process in an essentially harmonic well, since the value of α_2^i , the non-Gaussianity parameter for each particle i , is close to zero for almost all particles (just a few particles displaying significant deviations). Thus, in the approximation that each particle obeys Gaussian statistics we can write $\langle r_i^4 \rangle = 5/3 \langle r_i^2 \rangle^2$ and Eq. (15) becomes

$$\alpha_2 = N \frac{\sum_i \langle r_i^2 \rangle^2}{(\sum_i \langle r_i^2 \rangle)^2} - 1. \quad (16)$$

For homogeneous systems, (i.e., when all particles experience the same confining harmonic potential) $\langle r_i^2 \rangle = \langle r^2 \rangle$ and the last equation would yield $\alpha_2=0$. Hence, the nonergodicity observed in the dynamics of the fully connected gels is a signature of the heterogeneities of the dynamics induced by heterogeneities in the structural properties.

1. Self and collective scattering function

We study the behavior of the self-density fluctuations $F_s(q, t)$ in the network state for majority particles (three functional for $x_2=0.2$ and bifunctional for $x_2=0.9$) for different wave vectors \vec{q} ,

$$F_s(q, t) \equiv \left\langle \frac{1}{N} \sum_i e^{-i\vec{q} \cdot (\vec{r}_i(t) - \vec{r}_i(0))} \right\rangle. \quad (17)$$

Figure 11(a) shows $F_s(q, t)$ at different wave vectors. The correlation decays to a plateau, whose height f_q is wave vector dependent, signaling the nonergodic state of the sys-

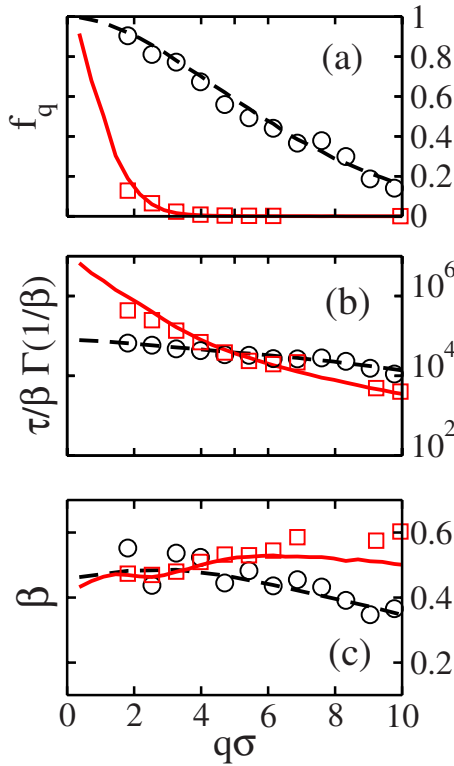


FIG. 12. Fit results for systems $x_2=0.2$ [dashed line for the incoherent scattering function $F_s(q,t)$ and circles for the coherent scattering function $F_c(q,t)$] and $x_2=0.9$ [solid line for $F_s(q,t)$ and squares for $F_c(q,t)$]: (a) Nonergodicity factor, (b) area under the stretched exponential curve, and (c) stretched exponent. The results for the collective scattering function start from $q\sigma=1.81$ because the bad statistics at low- q do not permit sensitive fits.

tem, which retains even at very long times the memory of the initial state. Different from glasses, where all q vectors are nonergodic, for this system f_q goes to zero with continuity at high q vectors. In fact, the nonergodicity shows up in gels only above a certain length scale.

The decay of $F_s(q,t)$ after the initial ballistic regime for $\bar{\tau} < 0.017$ (see Appendix) can be conveniently parametrized with a stretched exponential decay [continuous lines in Fig. 11(a)], i.e., with the function $f(t)$,

$$f(t) = f_q + A e^{-(t/\tau)^\beta}, \quad (18)$$

where f_q is the nonergodicity factor, A is the amplitude, τ is the decay parameter, and β is the stretched exponent.

The stretched exponential relaxation is ubiquitous in the description of both colloidal and polymer suspensions far beyond the sol-gel point and it is due to the hierarchy of intracuster elastic modes that contribute to the decay of density correlations.⁵⁰⁻⁵⁴

Figure 12 shows the results of the numerical fits for two average valences for q -vectors up to 10.85σ [for higher q vectors $F_s(q,t)$ decays to zero within the ballistic region and hence $F_s(q,t)$ provides only information on the microscopic ballistic single particle dynamics].

The q dependence of the nonergodicity factor f_q for the two limiting values of x_2 is shown in Fig. 12(a). The width of

this distribution significantly shrinks on increasing x_2 , providing the q -space analog of the plateau in the mean squared displacement (Fig. 8).

Figure 12(b) depicts the area under the fit curve, i.e., $\int A e^{-(t/\tau)^\beta} dt = \tau/\beta \Gamma(1/\beta)$, which represents a suitable and often used definition of a decay time for the stretched exponential relaxation. For small q , the dynamic is slower for systems with high x_2 since they have longer chains of bifunctional units (see Fig. 5) between the branching points, $\bar{\tau}$ is larger and more time is requested to sample the bond cage. For larger q , the observed length scale becomes comparable to the particle size and one observes the short-time motion of the single particle. In this condition, more bonded particles are less mobile and, as can be seen in Fig. 12(b), three-functional monomers become slower than bifunctional ones. This is a simple bond-caging effect which is more effective for higher-valence particles. The crossover between the two regimes happens at length scales comparable with the average distance between particles. Figure 12(c) displays the value of the stretching exponent β , which is always found significantly different from the Debye relaxation value ($\beta=1$), since there are no length scales at which the process appears diffusional.

The decay of $F_s(q,t)$ can be linked to the Van Hove self-correlation function by the following expansion:⁴⁹

$$F_s(q,t) = e^{-q^2 \rho_1(t)} \left[1 + \frac{1}{2!} \alpha_2(t) [q^2 \rho_1(t)]^2 - \frac{1}{3!} [\alpha_3(t) - 3 \alpha_2(t)] [q^2 \rho_1(t)]^3 + \dots \right], \quad (19)$$

where $\rho_1(t) = \langle r(t)^2 \rangle / 6$ and α_n are given in Eq. (14). The order 0 term is equivalent to the Gaussian approximation of the Van Hove function. Figure 11(b) shows the different terms of Eq. (19) for some particular low q vectors. Consistent with the analysis of the data in real space, the Gaussian approximation results in a poor approximation despite the small value of q . One has to resort to at least the second order correction to properly describe the decay of the correlation, except for very small q values. This non-Gaussian effect results from the structural inhomogeneities which affect the single particle dynamics.

To study the actual relaxation of the network we also considered the coherent (collective) intermediate scattering function as defined by

$$F_c(q,t) \equiv \frac{1}{NS(q)} \left\langle \sum_{ij} e^{-i\vec{q} \cdot (\vec{r}_i(t) - \vec{r}_j(0))} \right\rangle, \quad (20)$$

$F_c(q,t)$ behaves like the incoherent scattering function $F_s(q,t)$ with a stretched exponent relaxation to a plateau. The parameters obtained by fitting the relaxation of $F_c(q,t)$ with Eq. (18) are shown as symbols in Fig. 12. The results show substantial quantitative agreement with the values obtained from the incoherent scattering (lines in Fig. 12), thus confirming our previous analysis.

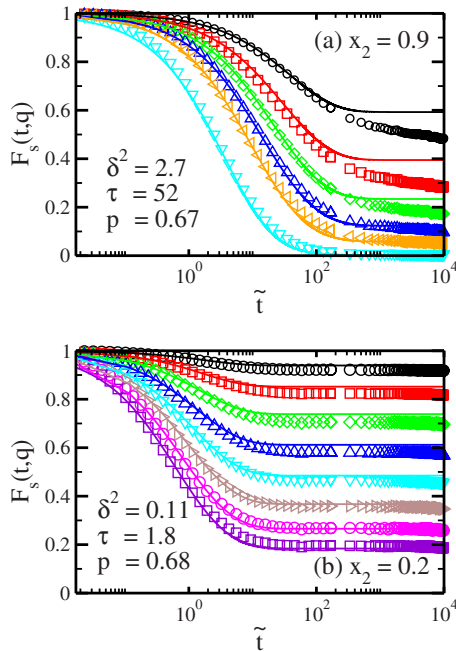


FIG. 13. Self-scattering functions fitted according to the Krall–Weitz model, Eq. (21), substituted in the first term of expansion of Eq. (19) with fitting parameters reported in the legend. (a) System with $x_2=0.9$ for scattering vectors (from top to bottom) $q\sigma=1.1, 1.4, 1.8, 2.2, 2.5, 3.6$. (b) System with $x_2=0.2$ for scattering vectors (from top to bottom) $q\sigma=1.8, 2.9, 4.0, 5.1, 6.2, 7.2, 8.3, 9.4$.

2. Krall–Weitz model for cluster dynamics

The Krall–Weitz⁵⁰ model has been very successful in characterizing the dynamics of fractal clusters and, for its general features, it has been extended to a variety of systems such as high density colloidal gels,^{51,52} polymer hydrogels,^{53,54} and computer simulations models.⁵⁵

The model takes into account the contribution of internal elastic modes of many length scales and predicts for a mode of length $\xi \sim q^{-1}$ the following mean square displacement:

$$\langle \Delta r_{\xi}^2(t) \rangle = \delta^2 [1 - e^{-(t/\tau)^p}], \quad (21)$$

where δ^2 is the plateau-height measuring the mean square displacement of the fractal cluster segments, τ is the characteristic decay time, and p is the decay exponent. The model relates the exponent p to the elasticity exponent β_e via the following relation: $p = \beta_e / (\beta_e + 1)$. For fractals the exponent β_e reflects the propensity for loops within the aggregate, since more loops result in a floppier cluster.

Figure 13 shows the results of the Krall–Weitz model for two systems, respectively, with the lowest ($x_2=0.9$) and highest ($x_2=0.2$) numbers of branching monomers. It shows that the model does capture the correct behavior for the relaxation of the scattering function with the same fitting parameters being valid for all q vectors for each system.

Interestingly the value of the p exponent is the same (within uncertainty) for both systems (and for all the x_2 fractions considered in this paper). Moreover the value $p \sim 0.7$ is the same obtained both for low-density fractal clusters⁵⁰ and for high density⁵² ($\phi=0.2$, two times the one considered in this article) gels made of polystyrene colloidal particles. It has been suggested⁵² that the exponent $p=0.07 \pm 0.05$ could

be a common feature of colloidal gels but experiments on colloidal silica⁵¹ found $p=0.5$ and computer simulations with the Asakura–Oosawa potential⁵⁵ reported $p=0.4$. Both studies suggested that the low p exponent could be related to a higher angular rigidity of the local network resulting in a structure less compliant on longer length scale. But different from these studies, our model directly incorporates angular rigidity of bonds through directional interactions without observing any decrease in the p exponent. Even more strikingly our p exponent remains unchanged for all x_2 systems and so it is not affected by the different connectivity of the network. The relation between p and the elasticity exponent β_e for high density systems is therefore unclear since with our model it is possible to explicitly calculate the number of loops in the network, Fig. 3. Since the p exponent does not change between systems displaying low and high numbers of network loops it cannot be related to the propensity for loops within the aggregate. Caution must then be taken with the physical interpretation of the Krall–Weitz model parameters for high density systems, where most of the scaling relations upon which the theory is based are not valid.

V. CONCLUSIONS

Patchy particles are an ideal model for the study of reversible gelation. By tuning the average valence it is possible to explore low-density states at low temperatures while avoiding the phase separation region. In this paper we have introduced a model for patchy particles based on a suitable continuous potential and investigated the role of the valence in the structure and dynamics of the low T gel.

First, we have shown that the connectivity properties are rather well described by the mean-field W and FS theories. A very good agreement is found for the T dependence of the bond probability (Fig. 2) and the distribution of chain lengths (Fig. 5) for all systems considered, except that in a small window of p_b values close to percolation, where the mean field universality class is expected to be replaced by the percolation universality class. The width of this nonmean field region increases with the average valence. Indeed, close to percolation the cluster size distributions are in good agreement with the theoretical results for the case of high x_2 while there are detectable deviations for the systems with a large fraction of three-functional particles (Fig. 4). Similarly, we observed that the number of loops in nonpercolating clusters (Fig. 3), which are assumed to be absent in both the W and FS theories, is negligible for $x_2=0.9$ but detectable in the $x_2=0.2$ systems. At low T , when $p_b \rightarrow 1$, the mean field predictions are always correct and it is thus possible to provide a quantitative analysis of the gel structure in terms of chains of two-functional particles connecting the branching points. The different gel structures obtained by varying the average valence were characterized by calculating the radial distribution function [Fig. 6(a)] and the static structure factor [Fig. 6(b)], respectively, showing the conformation of chains and the approach of (gas-liquid) thermodynamic instabilities when the average valence approaches three (at the studied ϕ).

We have also investigated the dynamics in the network

in the low T case, where all particles belong to one spanning cluster and thus the dynamics can be attributed to the intrinsic modes of the network. The mean square displacement (Fig. 8) shows the crossover to a plateau whose height is the value of the localization length (l_0) of particles in the arrested structure. The localization length is higher than one would expect from just the cage effect of neighboring particles or from the bond distance and grows significantly by lowering the average valence of the system. This behavior is due to the fact that while being bonded to neighbors, particles participate to the floppy modes of the network, whose amplitudes strongly depend on the average chain length. Moreover a precise relation between the mean square displacement of three-functional and bifunctional monomers is found, the ratio being precisely $2/3$ for all valences studied. This is an important property of the whole network fluctuations, whose behavior resembles the one predicted by the phantom model of polymer gels, an agreement probably favored by the small packing fraction of the studied system. Further work is requested in this respect, and we plan to investigate the validity of the phantom model predictions upon changing three-functional particles with particles with higher functionality (keeping the average valence constant). We also plan to explore the effect of density on the low- T gel dynamics.

The Van Hove correlation function after the initial time scale becomes time invariant, giving us important information on the shape of the potential confining the particles in the network state. We find that the non-Gaussianity of this confining potential becomes more pronounced as the three-functional particles are added to the system and the network becomes more entangled. The origin of the non-Gaussianity is traced back to the heterogeneities in the local structure.

Complementary information on the way particles explore the accessible space is also encoded in the time dependence of the self-intermediate scattering function. For wave vectors smaller than $2\pi/l_0$ we find that the system displays nonergodic behavior with the scattering function approaching a plateau, just as in real space the mean square displacement reaches l_0^2 . The wave vector dependence of f_q shows a significant dependence on the valence. Nonergodic behavior ($f_q > 0$) is observable in a range of q which shrinks on decreasing the average valence. The approach to the plateau value (Fig. 11) is well represented by a stretched exponential relaxation. The decay time of the stretched relaxation shows a strong dependence on the average valence. At small q , where $F_s(q, t)$ probes the dynamics of the exploration of space over distances l_0 , the low x_2 systems relax more slowly because the network of particles is composed of longer bifunctional chains and hence larger l_0 . For large q , where $F_s(q, t)$ probes motions over distances comparable or smaller than the particles size, the opposite effect is observed due to the fact that higher bonded particles are more confined.

We also applied the Krall–Weitz model to our systems finding strong analogies with experimental studies on gels of polystyrene colloidal particles.^{50,52} The value of the elasticity exponent is found to be constant over the whole range of examined valences, thus asserting the independence of the elastic constant exponent p on the network entanglement.

In summary, results reported in this articles show that by tuning the valence of systems of patchy particles it is possible to tailor the gel properties, and that these can be effectively predicted using W and FS theories. At the same time, the low T gel, generated via slowly cooling of a physical gel model, has a structure which may well be very similar to the one of chemically cross-linked polymeric gels, where the number of crosslink plays the same role as the number of three-functional particles. Besides the recently reported analogies between physical and chemical gels in their aggregation kinetics,^{30,31} also significant analogies in the gel dynamics of physical and chemical gels are expected. Work in this direction is underway.

ACKNOWLEDGMENTS

We thank C. De Michele, E. Zaccarelli, E. Bianchi, and P. G. De Sanctis Lucentini for helpful discussions, F. Romano for help with data fits, and L. Rovigatti for double checking the numerical analysis. We acknowledge support from NoE SoftComp (Grant No. NMP3-CT-2004–502235).

APPENDIX: BROWNIAN ALGORITHM

The Brownian algorithm used in the simulations is a modification of the one described in Ref. 56. In the latter algorithm the particles undergo random collisions with the thermostat every t_0 time steps. This is implemented by extracting the velocity of each particle from the Maxwell–Boltzmann distribution at the thermostat temperature. The free-flight motion of colloids is calculated using a symplectic reversible integrator.⁵⁷ While producing the correct diffusive motion of the system, the algorithm yields an unphysical decorrelation of all particle's velocities every t_0 time steps.

To avoid this problem we define a probability (p) for each particle to undergo a random collision each time step. In this way the time t between two random collisions is a stochastic variable having the following probability distribution: $p(t) = p(1-p)^{(t-1)}$. Limiting the discussion to a one-dimensional case, the position of a particle can then be written as $X(N) = X_1 + X_2 + \dots + X_N$, where X_i is the displacement after the i th random collision. We now write $X_i = T_i V_i$, where T_i is the time interval between the i th and $(i+1)$ th collisions and V_i is the velocity after the i th collision. Dropping the i subscript, the probability distribution for the variable X can be written as $p_X(x) = \int \int p_T(t) p_V(v) \delta(vt - x) dt dv$ or $p_X(x) = \int_0^\infty p_T(t) p_V(x/t) / t dt$. The second moment of the distribution is $\sigma^2 = 2 \int_0^\infty x^2 p_X(x) dx$. Substituting the previous expressions and remembering that $p_V(v)$ is the Maxwell–Boltzmann distribution, $p_V(v) = \sqrt{m/2\pi k_B T} \exp(-mv^2/2k_B T)$, we get $\sigma^2 = k_B T \langle T^2 \rangle / m$. The diffusion coefficient can be calculated by means of Einstein's equation $D = \langle X^2(\Delta t) \rangle / 2\Delta t = N \sigma^2 / (2N \langle T \rangle) = (k_B T / 2m) \langle T^2 \rangle / \langle T \rangle$. Using the aforementioned probability distribution for the collision times we get the following expression for the diffusion coefficient: $D = (k_B T / 2m) (2 - 3p + p^2) / ((1-p)p)$. This formula shows that by tuning the probability p it is possible to obtain the desired diffusion coefficient.

For efficiency reasons it is best to perform random

collisions not each time step, but every N time step. Therefore every $N\delta t$ unit of time (where δt is the time step of the algorithm) a particle has a probability p of undergoing a Brownian collision. This means that the average time between two random collisions is given by $t=N\delta t/p=(k_B TN\delta t+2mD)/2k_B T$. For the low temperature simulations (with $N=50$) we have, on average, two collisions after $t=0.278$ ($\tilde{\tau}=0.017$). Thus our simulations follow a Newtonian dynamics for $\tilde{\tau}<0.017$ and a Brownian dynamics after that time. All fits shown in this article are for times in the Brownian regime $\tilde{\tau}>0.017$. With the choice of the thermostat parameters we thus assure that the average distance between two successive collisions is less than the range of the potential of interaction between the particles, so that the collision process is described by Brownian statistics. During the Newtonian regime the particle travels a distance of 0.096 while the range of the potential is 0.125 in units of the particle diameter. See, for example, Ref. 29 where with the same algorithm the correct Smoluchowski–Brownian aggregation rate is recovered.

The same considerations also hold for the rotational motion of particles. We thus introduce a probability (p_r) for a colloid to undergo a rotational collision extracting its angular velocity from a Maxwell–Boltzmann distribution. For spheres with no-slip boundary conditions the rotational diffusion coefficient (D_r) is related to the translational diffusion by the equation $D_r=3/\sigma^2 D$, which can be realized by appropriately choosing p_r .

- ¹E. Zaccarelli, S. V. Buldyrev, E. La Nave, A. J. Moreno, I. Saika-Voivod, F. Sciortino, and P. Tartaglia, *Phys. Rev. Lett.* **94**, 218301 (2005).
- ²E. Del Gado and W. Kob, *Europhys. Lett.* **72**, 1032 (2005).
- ³R. Blaak, M. A. Miller, and J.-P. Hansen, *Europhys. Lett.* **78**, 26002 (2007).
- ⁴P. I. Hurtado, L. Berthier, and W. Kob, *Phys. Rev. Lett.* **98**, 135503 (2007).
- ⁵E. Zaccarelli, *J. Phys.: Condens. Matter* **19**, 323101 (2007).
- ⁶F. Sciortino, S. Buldyrev, C. De Michele, N. Ghofraniha, E. La Nave, A. Moreno, S. Mossa, P. Tartaglia, and E. Zaccarelli, *Comput. Phys. Commun.* **169**, 166 (2005).
- ⁷P. J. Lu, E. Zaccarelli, F. Ciulla, A. B. Schofield, F. Sciortino, and D. A. Weitz, *Nature (London)* **453**, 499 (2008).
- ⁸S. Buzzaccaro, R. Rusconi, and R. Piazza, *Phys. Rev. Lett.* **99**, 098301 (2007).
- ⁹S. Mossa, F. Sciortino, P. Tartaglia, and E. Zaccarelli, *Langmuir* **20**, 10756 (2004).
- ¹⁰A. Coniglio, L. DeArcangelis, E. Del Gado, A. Fierro, and N. Sator, *J. Phys.: Condens. Matter* **16**, S4831 (2004).
- ¹¹F. Sciortino, P. Tartaglia, and E. Zaccarelli, *J. Phys. Chem. B* **109**, 21942 (2005).
- ¹²M. Tarzia and A. Coniglio, *Phys. Rev. E* **75**, 011410 (2007).
- ¹³E. Zaccarelli, S. Andreev, F. Sciortino, and D. R. Reichman, *Phys. Rev. Lett.* **100**, 195701 (2008).
- ¹⁴J. Wu, Y. Liu, W. Chen, J. Cao, and S. Chen, *Phys. Rev. E* **70**, 050401 (2004).
- ¹⁵J. C. Fernandez Toledano, F. Sciortino, and E. Zaccarelli, *Soft Matter* **5**, 2390 (2009).
- ¹⁶I. Saika-Voivod, E. Zaccarelli, F. Sciortino, S. V. Buldyrev, and P. Tartaglia, *Phys. Rev. E* **70**, 041401 (2004).
- ¹⁷E. Michel, M. Filali, R. Aznar, G. Porte, and J. Appell, *Langmuir* **16**, 8702 (2000).

- ¹⁸R. Johannsson, C. Chassenieux, D. Durand, T. Nicolai, P. Vanhoorne, and R. Jerome, *Macromolecules* **28**, 8504 (1995).
- ¹⁹E. Bianchi, J. Largo, P. Tartaglia, E. Zaccarelli, and F. Sciortino, *Phys. Rev. Lett.* **97**, 168301 (2006).
- ²⁰E. Bianchi, P. Tartaglia, E. La Nave, and F. Sciortino, *J. Phys. Chem. B* **111**, 11765 (2007).
- ²¹E. Vakarin, Y. Duda, and M. F. Holovko, *Mol. Phys.* **90**, 611 (1997).
- ²²F. Sciortino, *Eur. Phys. J. B* **64**, 505 (2008).
- ²³F. W. Starr and F. Sciortino, *J. Phys.: Condens. Matter* **18**, L347 (2006).
- ²⁴J. P. K. Doye, A. A. Louis, I.-C. Lin, L. R. Allen, E. G. Noya, A. W. Wilber, H. C. Kok, and R. Lyus, *Phys. Chem. Chem. Phys.* **9**, 2197 (2007).
- ²⁵S. C. Glotzer and M. J. Solomon, *Nature Mater.* **6**, 557 (2007).
- ²⁶A. Hiddessen, S. Rodgers, D. Weitz, and D. Hammer, *Langmuir* **16**, 9744 (2000).
- ²⁷V. T. Milam, A. Hiddessen, S. Rodgers, and J. C. Crocker, *Langmuir* **19**, 10317 (2003).
- ²⁸A. Hiddessen, D. Weitz, and D. Hammer, *Langmuir* **20**, 6788 (2004).
- ²⁹N. Ghofraniha, P. Androzzzi, J. Russo, C. L. Mesa, and F. Sciortino, *J. Phys. Chem. B* **113**, 6775 (2009).
- ³⁰S. Corezzi, C. De Michele, E. Zaccarelli, D. Fioretto, and F. Sciortino, *Soft Matter* **4**, 1173 (2008).
- ³¹S. Corezzi, C. De Michele, E. Zaccarelli, P. Tartaglia, and F. Sciortino, *J. Phys. Chem. B* **113**, 1233 (2009).
- ³²E. Bianchi, P. Tartaglia, E. Zaccarelli, and F. Sciortino, *J. Chem. Phys.* **128**, 144504 (2008).
- ³³M. Wertheim, *J. Stat. Phys.* **35**, 19 (1984); **35**, 35 (1984).
- ³⁴M. Wertheim, *J. Stat. Phys.* **42**, 459 (1986); **42**, 477 (1986).
- ³⁵P. J. Flory, *Principles of Polymer Chemistry* (Cornell University Press, Ithaca, 1953).
- ³⁶F. Sciortino, C. De Michele, S. Corezzi, J. Russo, E. Zaccarelli, and P. Tartaglia, *Soft Matter* **5**, 2571 (2009).
- ³⁷J. P. Hansen and I. R. McDonald, *Theory of Simple Liquids*, 3rd ed. (Academic, New York, 2006).
- ³⁸G. Jackson, W. G. Chapman, and K. E. Gubbins, *Mol. Phys.* **65**, 1 (1988).
- ³⁹D. Chandler and L. R. Pratt, *J. Chem. Phys.* **65**, 2925 (1976).
- ⁴⁰W. H. Press, B. P. Flannery, S. A. Teukolsky, and W. T. Vetterling, *Numerical Recipes in Fortran* (Cambridge University Press, Cambridge, 1999).
- ⁴¹A. Coniglio and W. Klein, *J. Phys. A* **13**, 2775 (1980).
- ⁴²C. Padoa-Schioppa, F. Sciortino, and P. Tartaglia, *Phys. Rev. E* **57**, 3797 (1998).
- ⁴³B. A. H. Huisman, P. G. Bolhuis, and A. Fasolino, *Phys. Rev. Lett.* **100**, 188301 (2008).
- ⁴⁴D. Stauffer and A. Aharony, *Introduction to Percolation Theory*, 2nd ed. (Taylor & Francis, London, 1992).
- ⁴⁵D. Stauffer, A. Coniglio, and M. Adam, *Adv. Polym. Sci.* **44**, 193 (1982).
- ⁴⁶C. P. Lusignea, T. H. Mourey, J. C. Wilson, and R. H. Colby, *Phys. Rev. E* **60**, 5657 (1999).
- ⁴⁷H. M. James, *J. Chem. Phys.* **15**, 651 (1947).
- ⁴⁸H. M. James and E. Guth, *J. Chem. Phys.* **15**, 669 (1947).
- ⁴⁹J. P. Boon and S. Yip, *Molecular Hydrodynamics* (McGraw-Hill, New York, 1980).
- ⁵⁰A. H. Krall and D. A. Weitz, *Phys. Rev. Lett.* **80**, 778 (1998).
- ⁵¹M. J. Solomon and P. Varadan, *Phys. Rev. E* **63**, 051402 (2001).
- ⁵²S. Romer, F. Scheffold, and P. Schurtenberger, *Phys. Rev. Lett.* **85**, 4980 (2000).
- ⁵³P. Barretta, F. Bordini, C. Rinaldi, and G. Paradossi, *J. Phys. Chem. B* **104**, 11019 (2000).
- ⁵⁴F. Bordini, G. Paradossi, C. Rinaldi, and B. Ruzicka, *Physica A* **304**, 119 (2002).
- ⁵⁵R. J. D'Arjuzon, W. Frith, and J. R. Melrose, *Phys. Rev. E* **67**, 061404 (2003).
- ⁵⁶F. Sciortino, C. De Michele, and J. F. Douglas, *J. Phys.: Condens. Matter* **20**, 155101 (2008).
- ⁵⁷A. Dullweber, B. Leimkuhler, and R. McLachlan, *J. Chem. Phys.* **107**, 5840 (1997).